



**Repositorio Institucional de la Universidad Autónoma de Madrid**

<https://repositorio.uam.es>

Esta es la **versión de autor** del artículo publicado en:

This is an **author produced version** of a paper published in:

The Journal of Physical Chemistry Letters 6.1 (2015): 72-76

**DOI:** <http://dx.doi.org/10.1021/jz5022894>

**Copyright:** © 2014 American Chemical Society

El acceso a la versión del editor puede requerir la suscripción del recurso

Access to the published version may require subscription

# Nonadiabatic Quantum Dynamics Predissociation of $\text{H}_2\text{O}^+(\tilde{B}^2\text{B}_2)$

Jaime Suárez, L. Méndez, and I. Rabadán\*

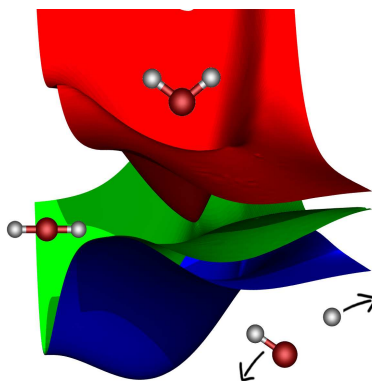
*Laboratorio Asociado al CIEMAT de Física Atómica y Molecular en Plasmas de Fusión.*

*Departamento de Química, módulo 13, Universidad Autónoma de Madrid, 28049-Madrid,  
Spain.*

E-mail: ismanuel.rabadan@uam.es

## Abstract

A quantum-mechanical study of the predissociation of  $\text{H}_2\text{O}^+(\tilde{B}^2\text{B}_2)$  is carried out by using wave packet propagations on *ab initio* potential energy surfaces connected by nonadiabatic couplings. The simulations show that within the first 30 fs, 80% of the initial wave packet is transferred from the  $\tilde{B}^2\text{B}_2$  to the  $\tilde{A}^2\text{A}_1$  electronic state through a conical intersection. A much slower transfer (in the ps timescale) from the  $\tilde{A}^2\text{A}_1$  to the  $\tilde{X}^2\text{B}_1$  state due to a Renner-Teller coupling determines the fragmentation branching ratios, which are in accordance with the experimental measurements.



---

\*To whom correspondence should be addressed

Keywords: Water cation, fragmentation, ab initio potentials, wave packet propagations, branching ratio, conical intersection.

The ionization of water molecules and the ensuing fragmentation, which yields the singly charged ions  $\text{H}^+$ ,  $\text{OH}^+$  and  $\text{O}^+$ , are relevant processes in several fields. In astrophysics, for example, the water cation has been detected in the interstellar medium,<sup>1,2</sup> molecular clouds, planetary atmospheres and cometary comae;<sup>3</sup> the breakdown of the water cation takes place in the atmospheres of icy moons.<sup>4</sup> The ionization of  $\text{H}_2\text{O}$  is also a primary reaction in radiation-induced damage of biological systems. In particular, high energy ions ( $\text{H}^+$  or  $\text{C}^{6+}$ ), used in ion-beam-cancer therapy ionize the water molecules of the cytoplasm, yielding electrons, radicals and ions, which interact with the DNA in secondary processes. In this context, several works<sup>5–7</sup> have estimated the branching ratios for production of the cations  $\text{H}_2\text{O}^+$ ,  $\text{H}^+$ ,  $\text{OH}^+$  and  $\text{O}^+$  in ion- $\text{H}_2\text{O}$  collisions by combining the experimental  $\text{H}_2\text{O}^+$  breakdown probabilities<sup>8</sup> with theoretical calculations of single-electron removal from  $\text{H}_2\text{O}$ . The good agreement between these semiempirical results and the experiments<sup>9–12</sup> indicates that the ions  $\text{H}^+$ ,  $\text{OH}^+$  and  $\text{O}^+$  are formed through a two-step mechanism that involves the ionization of  $\text{H}_2\text{O}$  followed by the post-collisional fragmentation of  $\text{H}_2\text{O}^+$ .

The fragmentation mechanism of  $\text{H}_2\text{O}^+$  has been studied in several publications. Early theoretical and experimental works<sup>13–15</sup> showed that the photoionization of water with photons of energy lower than 21.2 eV leads to the population of the electronic states  $\tilde{X}^2\text{B}_1$ ,  $\tilde{A}^2\text{A}_1$  and  $\tilde{B}^2\text{B}_2$  of  $\text{H}_2\text{O}^+$ . The energies of the vibronic states formed by vertical ionization into  $\tilde{X}$  and  $\tilde{A}$  electronic states lie below the dissociation threshold, while vibrational states with energies above the dissociation channels  $\text{H}(1s)+\text{OH}^+(\text{X}^3\Sigma^-)$  and  $\text{H}^++\text{OH}(\text{X}^2\Pi)$  can be populated in the ionization into the  $\tilde{B}$  state. The dissociation of  $\text{H}_2\text{O}^+(\tilde{B}^2\text{B}_2)$  leading to  $\text{H}(1s)+\text{OH}^+(\text{X}^3\Sigma^-)$  could take place either via nonadiabatic (spin-orbit) transitions to the dissociative  $\tilde{a}^4\text{B}_1$  state, or by transitions to the vibrational continuum of the ground state,  $\tilde{X}^2\text{B}_1$ . The dissociation into  $\text{H}^++\text{OH}$  involves  $\tilde{B} \rightarrow \tilde{A}$  transitions. The branching ratios for dissociation into the different channels were measured by Tan et al.<sup>8</sup> in combined (e,2e) and

(e,e+ion) experiments with electron energies of up to 60 eV. For collisional energies above 30 eV, the breakdown scheme is summarized in the following equations:<sup>8</sup>

$$\sigma^{\text{H}_2\text{O}^+} = 1.0 \sigma(1b_1) + 1.0 \sigma(3a_1) + 0.08 \sigma(1b_2) \quad (1)$$

$$\sigma^{\text{OH}^+} = 0.7 \sigma(1b_2) \quad (2)$$

$$\sigma^{\text{H}^+} = 0.22 \sigma(1b_2) + 0.74 \sigma(2a_1) \quad (3)$$

$$\sigma^{\text{O}^+} = 0.26 \sigma(2a_1), \quad (4)$$

which relate the total cross sections for the formation of  $\text{H}_2\text{O}^+$ ,  $\text{H}^+$ ,  $\text{OH}^+$  and  $\text{O}^+$  with the one-electron removal cross sections,  $\sigma(m)$ , from the valence molecular orbitals of  $\text{H}_2\text{O}$ ,  $m = 1b_1, 3a_1, 1b_2, 2a_1$ . The numerical coefficients are the experimental branching ratios.

The photoelectron spectrum of water<sup>16</sup> pointed out the main nonadiabatic transitions that could be involved in the dissociation of  $\text{H}_2\text{O}^+(\tilde{B} \ ^2\text{B}_2)$ , namely the transitions in the conical intersection (CI) between the potential energy surfaces (PES)  $\tilde{B}$  and  $\tilde{A}$ , and the Renner-Teller (RT) coupling between the states  $\tilde{A}$  and  $\tilde{X}$ . High-resolution photoelectron spectra have been reported by Reutt et al.,<sup>17</sup> and the structure of these spectra has been reproduced by the multiconfiguration time-dependent Hartree calculations of Eroms et al..<sup>18</sup> The transitions in the vicinity of the CI seam between  $\tilde{B}$  and  $\tilde{A}$  states have also been studied in the surface hopping calculations of Dehareng.<sup>19</sup>

The photoelectron-photoion experiments of Powis and Reynolds<sup>20</sup> showed an important rotational excitation of the fragments  $\text{OD}^+$  and  $\text{OD}$  formed in the dissociation of  $\text{D}_2\text{O}^+(\tilde{B} \ ^2\text{B}_2)$ ; this excitation was attributed to the dissociation mechanism involving, as a first step, a bending motion in which the ion approaches the region of nuclear coordinates close to the  $\tilde{B}$ - $\tilde{A}$  CI seam. The predissociation of the  $\tilde{B}$  state has been studied<sup>21</sup> using *ab initio* potential energy surfaces but, to our knowledge, no dynamical calculation has been carried out to determine the branching ratios to the different dissociation channels. Recently, Harbo et al.<sup>22</sup> performed photoabsorption experiments to measure the lifetime of

$\text{H}_2\text{O}^+(\tilde{B}^2\text{B}_2)$ . These authors also report the fragmentation branching ratios after the absorption of 532 nm laser light.

The present work targets the theoretical calculation of  $\text{H}_2\text{O}^+(\tilde{B}^2\text{B}_2)$  fragmentation probabilities by means of 3D wave packet propagations on several PESs. Both PESs and nonadiabatic couplings have been obtained *ab initio* using the program Molpro.<sup>23</sup> In particular, we have carried out multireference configuration interaction calculations in the  $\text{C}_s$  symmetry with 7 valence electrons in (7a',1a'') orbitals obtained from CASSCF calculations in a space of (10a',1a'') orbitals constructed using the aug-cc-pvqz basis set for oxygen and aug-cc-pvtz for hydrogen atoms.

In order to illustrate the fragmentation mechanism, we show in Figure 1(a) the cut of the PESs as function of the bond length  $r_2$ , for fixed bond angle  $\alpha = 104.6^\circ$  and  $r_1 = 1.788$  bohr, corresponding to the equilibrium geometry of  $\text{H}_2\text{O}$ . The vertical bar indicates the extension of the initial wave packet, obtained by a Franck-Condon (FC) transition from the  $\text{H}_2\text{O}$  ground state. The overlap between this relatively narrow initial wave function and the  $\tilde{B}$  excited vibrational states is very small and, therefore, above-the-barrier and tunneling dissociation mechanisms are negligible. This suggests that the nonadiabatic transitions are responsible for the breakdown reactions. Moreover, for this particular geometry, we observe a crossing between the curves of states  $\tilde{B}$  and  $\tilde{A}$ , where spin-orbit transitions can take place.

As the angle  $\alpha$  decreases, see Figure 1(b), the potential energy curves of states  $\tilde{B}$  and  $\tilde{A}$  approach each other until the CI between the corresponding PESs is formed. The energy of the  $\tilde{A}$  state decreases rapidly as  $\alpha$  increases, and becomes degenerate with the ground state  $\tilde{X}$  in the limit  $\alpha = 180^\circ$ , where they are the two components of a  $^2\Pi_u$  state.

The nonadiabatic transitions  $\tilde{B} \rightarrow \tilde{A}$  near the CI provide an efficient mechanism for depopulating the  $\tilde{B}$  state and, eventually, lead to the fragmentation of the molecular ion. Since this CI appears in the  $\text{C}_{2v}$  symmetry ( $r_1 = r_2$ ), we have employed the symmetry coordinates  $x = (r_1 + r_2)/2$  and  $y = (r_1 - r_2)/2$  to analyze the PESs and nonadiabatic couplings. In Figure 2 we have plotted the contour plots in the  $y = 0$  plane of the PES of

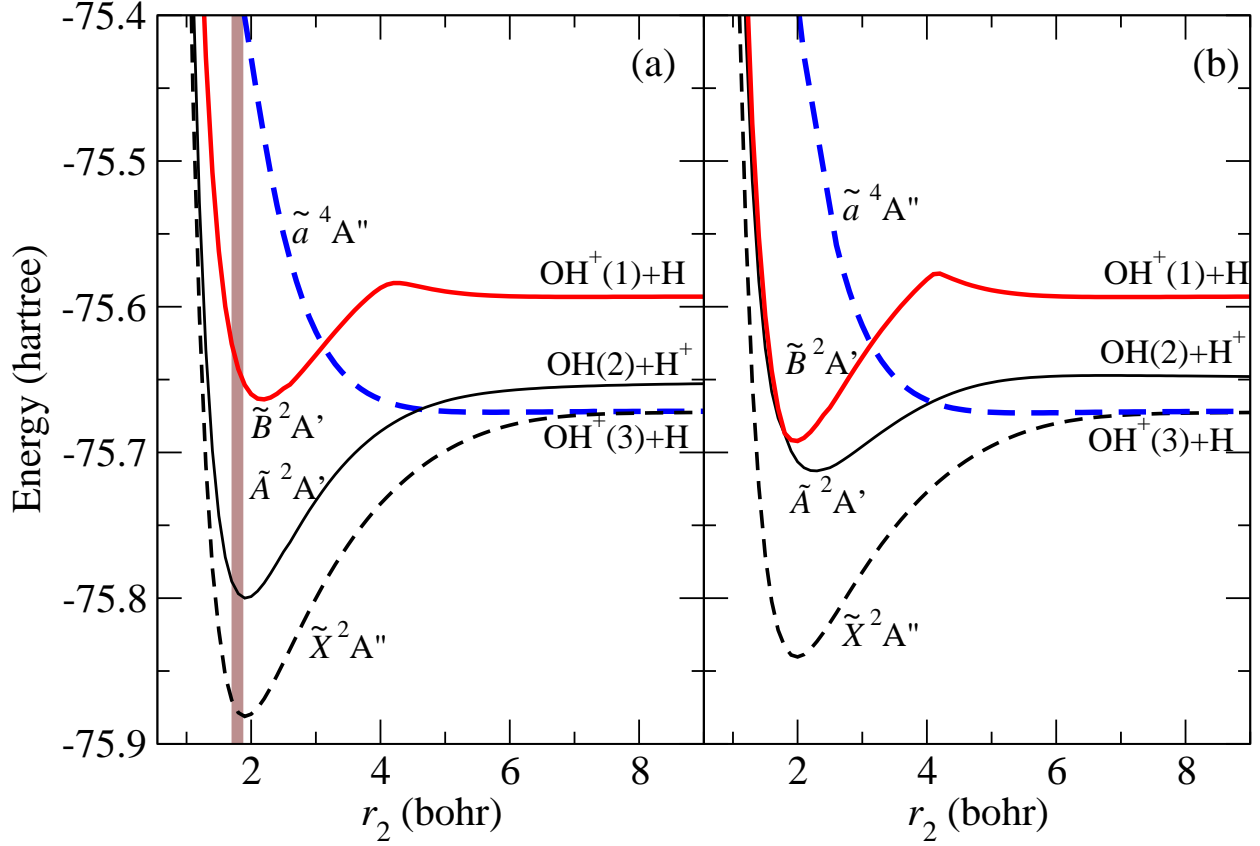


Figure 1: Potential energy curves of the  $\text{H}_2\text{O}^+$  system as functions of one O–H bond length ( $r_2$ ), while fixing the other O–H bond ( $r_1 = 1.788$  bohr) and the  $\widehat{\text{HOH}}$  bond angle,  $\alpha$ . (a)  $\alpha = 104.6^\circ$ ; (b)  $\alpha = 70^\circ$ .  $\text{OH}^+(1)$ ,  $\text{OH}^+(3)$  and  $\text{OH}(2)$  label the states  $\text{OH}^+(^1\Sigma^+)$  and  $\text{OH}^+(^3\Sigma^-)$  and  $\text{OH}(^2\Pi)$ , respectively. In (a), the vertical bar indicates the extension of the initial FC wave packet. Solid and dashed lines distinguish between  $\text{C}_s$   $\text{A}'$  and  $\text{A}''$  states, respectively, while the  $\text{C}_{2v}$  labels are used for convenience.

these two states, and we have added the line that corresponds to the CI seam.

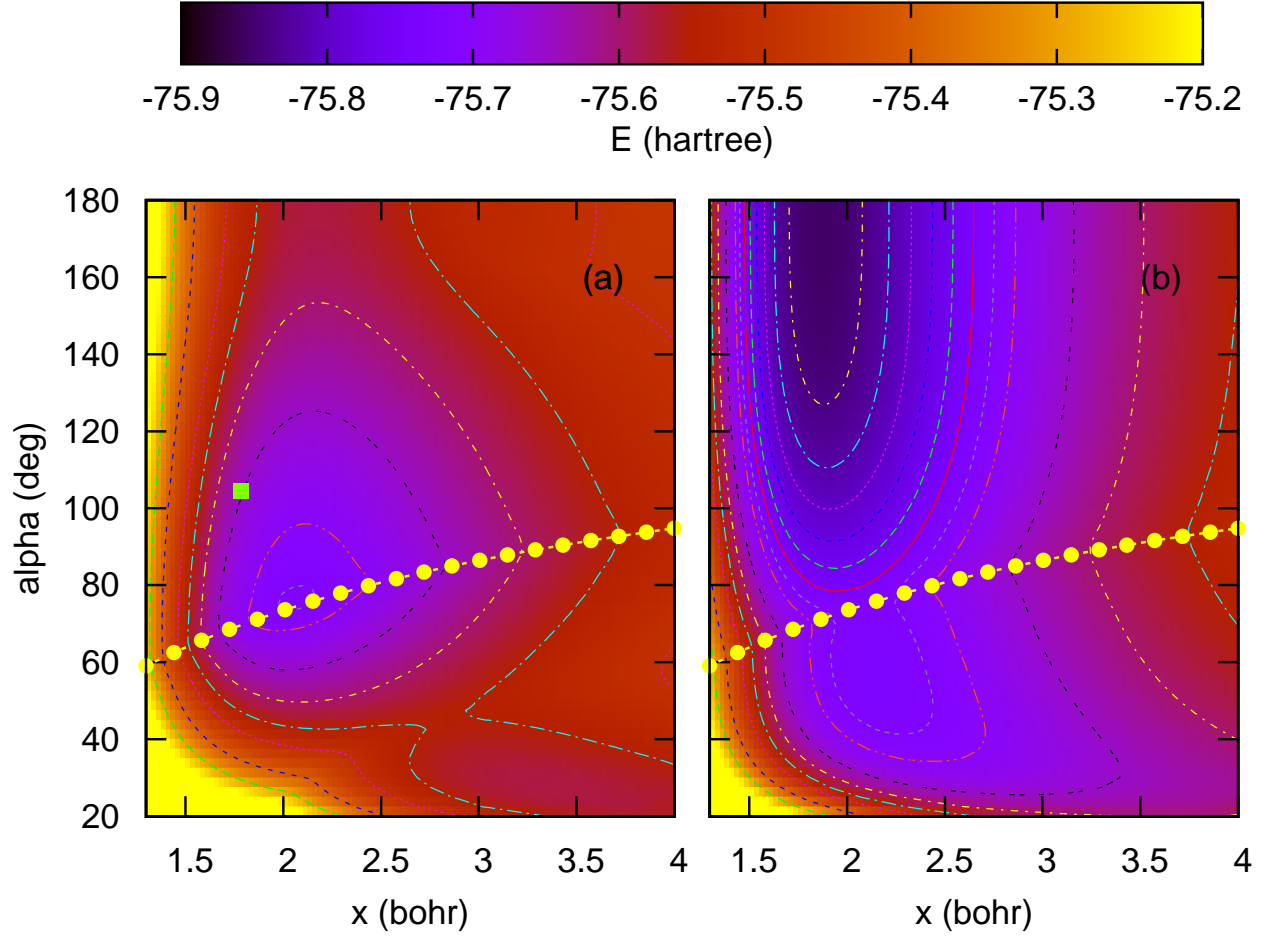


Figure 2: Contour plots of the adiabatic potential energy surfaces of the states (a)  $\tilde{B}^2B_2$  and (b)  $\tilde{A}^2A_1$  of  $H_2O^+$ , in the plane  $r_1 = r_2$ , as functions of the coordinate  $x = (r_1 + r_2)/2$  and  $\alpha$ , the bond angle  $\widehat{HOH}$ . The line with bullets marks the CI seam and the square in (a) the position of the maximum of the initial wave packet.

In practice, the wave packet propagation is carried out on a set of diabatic states, assuming that the nonadiabatic couplings in the diabatic basis vanish. The diabaticization procedure is particularly difficult near CIs because the nonadiabatic couplings diverge. In this work, we have carried out an adiabatic to diabatic transformation:

$$\mathbf{H}^d = \mathbf{U}^\dagger \mathbf{E} \mathbf{U} \quad ; \quad \mathbf{E} = \begin{pmatrix} E_1 & 0 \\ 0 & E_2 \end{pmatrix} \quad ; \quad \mathbf{U} = \begin{pmatrix} \cos \Theta & -\sin \Theta \\ \sin \Theta & \cos \Theta \end{pmatrix}, \quad (5)$$

where  $E_{1,2}$  are the adiabatic energies and the transformation angle,  $\Theta$ , is given by:

$$\tan 2\Theta = \frac{(0.00286\alpha^2 + 0.182\alpha + 1.54)y}{(\alpha - \alpha_{\text{CI}}) \cos(\pi\alpha'_{\text{CI}}/180)}, \quad (6)$$

with  $\alpha_{\text{CI}}(x) = \frac{80.27x}{1+0.592x}$  the location of the CI seam and  $\alpha'_{\text{CI}} = d\alpha_{\text{CI}}/dx$ . The numerical coefficients in eq. 6 have been calculated by fitting the model couplings, obtained by differentiating  $\Theta(x, y, \alpha)$ ,<sup>24</sup> to the *ab initio* nonadiabatic values. We illustrate the result of this procedure in Figure 3 by plotting several cuts of  $\partial\Theta/\partial q$  ( $q = x, y, \alpha$ ) and the gradient matrix elements  $\langle\varphi_{\tilde{B}}|\partial/\partial q|\varphi_{\tilde{A}}\rangle$ , where  $\varphi_{\tilde{B},\tilde{A}}$  denote the electronic wave functions of  $\tilde{B}$  and  $\tilde{A}$  states, respectively. With this diabatic model, the unitary transformation defined by eqs. 5 and 6 removes the singularities and the residual dynamical couplings are negligible.

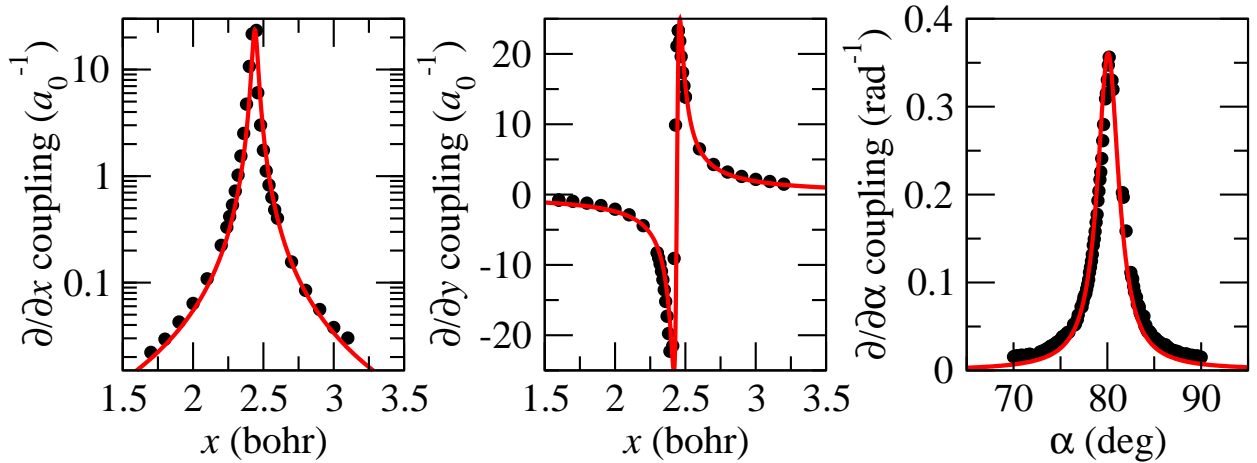


Figure 3: Comparison between the *ab initio* values of the dynamical couplings  $\langle\varphi_{\tilde{B}}|\partial/\partial q|\varphi_{\tilde{A}}\rangle$ ,  $q = x, y, \alpha$ , calculated with Molpro ( $\bullet$ ) and the derivatives  $\partial\Theta/\partial q$  (full lines). The left and middle panels display the  $x$ - and  $y$ -couplings as functions of  $x$  (with  $y = 0.01$  bohr and  $\alpha = 80^\circ$ ), while the right one shows the  $\alpha$ -coupling as a function of  $\alpha$  (with  $x = 2.45$  bohr and  $y = 0.05$  bohr).

Our treatment of  $\tilde{A}$ – $\tilde{X}$  transitions is based on the method of Haxton et al.,<sup>25,26</sup> in which, assuming a small total angular momentum, the Coriolis coupling terms are neglected and



the body-fixed Hamiltonian has the form:<sup>26,27</sup>

$$\begin{aligned}
H = & V(R, r, \theta) - \frac{\hbar^2}{2\mu_R} \frac{\partial^2}{\partial R^2} - \frac{\hbar^2}{2\mu_r} \frac{\partial^2}{\partial r^2} \\
& - \frac{1}{2} \left( \frac{1}{\mu_R R^2} + \frac{1}{\mu_r r^2} \right) \left( \frac{\hbar^2}{\sin \theta} \frac{\partial}{\partial \theta} \sin \theta \frac{\partial}{\partial \theta} - \frac{j_z^2}{\sin^2 \theta} \right)
\end{aligned} \tag{7}$$

where  $(R, r, \theta)$  are the Jacobi coordinates, being  $r$  the O–H distance.  $j_z$  is the  $z$  component of the angular momentum operator for the rotation of the diatom OH in the body-fixed frame, with  $\mathbf{R}$  along the  $\hat{z}$ -axis. In this approximation, the nuclear wave functions are assumed to be eigenfunctions of the body-fixed operator  $j_z$ . The operator  $j_z^2$  is substituted<sup>28</sup> into eq. 7 by its eigenvalues,  $\hbar^2 k^2$  ( $k = K - \Lambda$ ), which are only defined in the  $C_{\infty v}$  symmetry, where  $K$  and  $\Lambda$  are the quantum numbers for the  $z$  projections of the total and electronic angular momenta, respectively. In the present case, the electronic states  $\tilde{A}^2A_1$ ,  $\tilde{X}^2B_1$  correlate, in the limit  $\theta \rightarrow 180^\circ$ , with the two components of the  $^2\Pi_u$ , with  $|\Lambda| = 1$ . In this limit, the eigenfunctions of the  $z$  component of the electronic angular momentum operator with  $\Lambda = \pm 1$ ,  $\varphi_{\pm 1}$ , are linear combinations of the electronic wave functions,  $\varphi_{\tilde{A}, \tilde{X}}$ :

$$\varphi_{\pm 1} = \frac{1}{\sqrt{2}} (\varphi_{\tilde{A}} \pm i\varphi_{\tilde{X}}) \tag{8}$$

The non-diagonal matrix element of the potential in such diabatic representation, together with the kinetic energy operator term  $k^2/\sin^2 \theta$ , approximately account for the RT transitions.

The dissociation probabilities have been obtained by means of nuclear wave packet propagations on the diabatic electronic PESs, employing a computational method (GridTDSE)<sup>29</sup> that is naturally suited for massive parallel calculations. This technique consists of a direct numerical integration of the 3D time-dependent Schrödinger equation (TDSE):  $[H - i\hbar\partial/\partial t]\Psi(\mathbf{R}, t) = 0$  using lattice schemes.<sup>30</sup> In order to incorporate nonadiabatic transitions, we have modified the method by considering the wave function as a column vector  $\Psi$  with

components  $\{\Psi_i\}$ , where  $i$  labels the different (diabatic) electronic states included. The nuclear dynamics on each PES are now coupled through the interaction matrix elements  $H_{ij}^d(\mathbf{R})$ , which are: 1) the interaction matrix elements  $H_{12}^d$  of eq. 5; 2) the interaction between the RT pair  $\tilde{X}-\tilde{A}$ , due to the transformation in eq. 8; 3) the spin-orbit coupling, which has been introduced in exploratory calculations to gauge the effectiveness of the dissociation mechanism via population of the  $\tilde{a}$  state.

The calculations were carried out with a grid of 50 points in  $R \in [1, 7]$  bohr; 76 points in  $r \in [1.3, 7]$  bohr and 73 points in  $\theta \in [\epsilon, \pi - \epsilon]$  rad, with  $\epsilon = 2 \times 10^{-4}$ . In such a numerical integration scheme, the singularity at  $\sin \theta = 0$  can be eluded by evaluating  $\Psi$  on the surroundings of the troublesome points. We have included a mask function<sup>31</sup> in the propagation scheme to avoid nonphysical reflections in the grid walls; this mask function leads to a smooth decay of the wave packets for  $R, r > 6.0$  bohr. Following a procedure similar to that of Ma et al.,<sup>32</sup> the dissociation probabilities have been obtained by evaluating the outgoing flux at  $R, r = 6.0$  bohr for the adiabatic components of the wave-packet on each electronic state. Converge test with regard to the size of the grid were performed in exploratory two-dimensional  $(R, \theta)$  calculations finding small changes (less than 5%) in the final probabilities when the outgoing flux was evaluated at  $R = 10$  bohr.

A possible breakdown mechanism involves transitions from  $\tilde{B}$  to  $\tilde{A}$ , which then dissociates into  $\text{H}^+ + \text{OH}$ , and spin-orbit transitions to the state  $\tilde{a}$ , which dissociates into  $\text{OH}^+ + \text{H}$ , either directly,  $\tilde{B} \rightarrow \tilde{a}$ , or via a two-step process,  $\tilde{B} \rightarrow \tilde{A} \rightarrow \tilde{a}$ . We have carried out a 3-state  $\{\tilde{B}, \tilde{A}, \tilde{a}\}$  simulation with constant spin-orbit couplings of  $2 \times 10^{-4}$  hartree (the *ab initio* value obtained with Molpro near the crossing between the  $\tilde{A}$  and  $\tilde{a}$  PESs). In this 3-state calculation, the probability of dissociating into  $\text{H}^+ + \text{OH}$  is above 60%, while the production of  $\text{OH}^+ + \text{H}$  remains low ( $\approx 27\%$ ), due to the small magnitude of the spin-orbit coupling term. The main conclusion of these numerical simulations is that one has to include the transitions into the ground electronic state  $\tilde{X}$  in order to reproduce the experimental results of eqs. 1–4. Accordingly, we have carried out 3-state  $\{\tilde{B}, \tilde{A}, \tilde{X}\}$  dynamical calculations. In

the approximate treatment of the RT coupling explained above, the Hamiltonian depends on the quantum number  $k$ , with  $k = K$  for the  $\tilde{B}$  state and  $k = K \mp 1$  for the  $\varphi_{\pm}$  states defined in eq. 8. We have followed the evolution of the nuclear wave packet with  $K = 0, 1, \dots, 5$  and the results are shown in Figures 4 and 5.

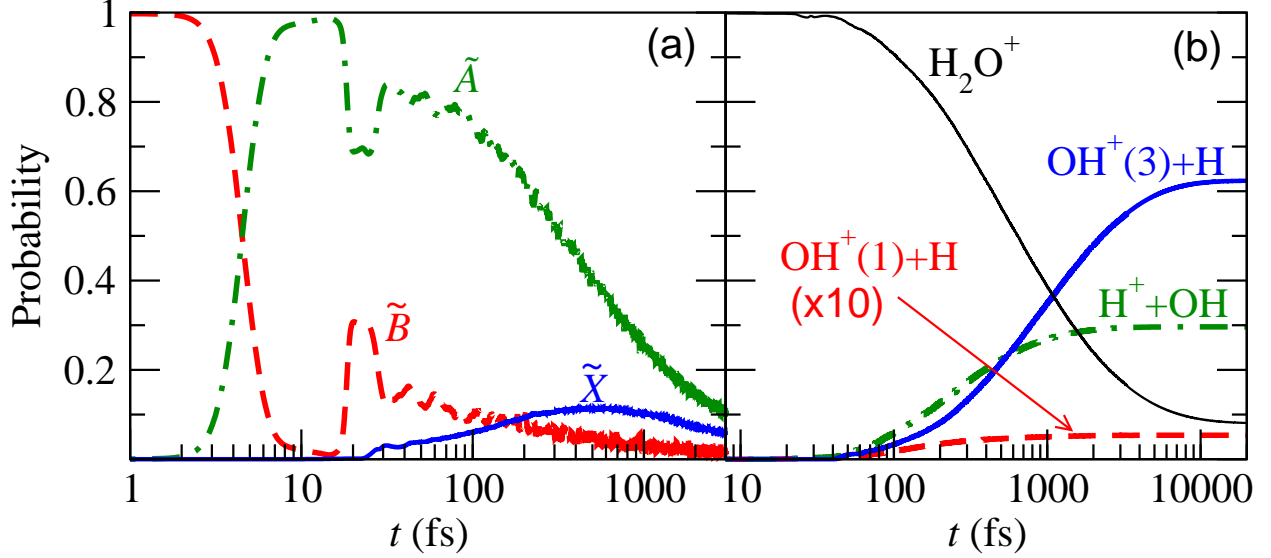


Figure 4: Time evolution corresponding to  $K = 1$  (see text) of (a) the populations of the  $\tilde{X}$ ,  $\tilde{A}$  and  $\tilde{B}$  electronic states of  $\text{H}_2\text{O}^+$ , as indicated in the graph, and (b) the probability of production of the different ions and radicals associated to the states of (a), with the same color and line style code; see also Figure 1. The breakdown into  $\text{OH}^+ + \text{H}$  has been multiplied by 10.

In Figure 4(a), we display the time evolution of the population of the vibrational bound states on the  $\tilde{X}$ ,  $\tilde{A}$  and  $\tilde{B}$  PESs of  $\text{H}_2\text{O}^+$  for  $K = 1$ . According to our results, the initial wave packet, originally at the  $\tilde{B}$  state, rapidly reaches the CI, where nearly 100% of it is transferred to the  $\tilde{A}$  state within the first 7 fs. During the following 10 fs, the wave packet evolves in the  $\tilde{A}$  PES showing a highly-excited bending motion, until it returns to the CI at  $t \approx 20$  fs; but, by that time, the wave packet has explored a broader region of the position space, and only about 1/3 of it returns to  $\tilde{B}$ . This part of the wave function spends another  $\approx 7$  fs on  $\tilde{B}$  before revisiting the CI and repopulating the  $\tilde{A}$  electronic state. From then on, part of the wave function is continuously being transferred to the  $\tilde{X}$  surface by the

Renner-Teller coupling, only efficient close to linear geometries, where the  $\tilde{A}$  PES minimum is located. Nevertheless, the rise of probability in  $\tilde{X}$  above 50 fs cannot completely account for the steady decline in both  $\tilde{A}$  and  $\tilde{B}$  populations, given the dissociative behavior of the wave packet. See Supporting Information for an animation of the first 160 fs of wave packet propagation.

Panel (b) of Figure 4 shows the probabilities of formation of the different ions and radicals, corresponding to the asymptotic limits of the three electronic states studied (see Figure 1). The fragmentation of  $\text{H}_2\text{O}^+$  is negligible during the first 50 fs, and starts almost simultaneously for both  $\text{H}^+$  and  $\text{OH}^+$  ions. The production of  $\text{H}^+ + \text{OH}$  moderately exceeds that of  $\text{OH}^+(3) + \text{H}$  during the first 500 fs, mainly because the population of  $\tilde{A}$  is much larger than that of  $\tilde{X}$ , which is only fed by the RT coupling with  $\tilde{A}$  at linear geometries. The fact that the production of  $\text{OH}^+$  clearly dominates at longer timescales indicates that the rate of fragmentation through the ground state  $\tilde{X}$  is larger than that of  $\tilde{A}$ . On the other hand, the contribution of  $\tilde{B}$  to the production of  $\text{OH}^+(1)$  is negligible at all times. The system reaches asymptotic conditions after 10 ps, when the fragmentation probabilities are 63% for production of  $\text{OH}^+(^3\Sigma^-) + \text{H}$  and 30% for  $\text{H}^+ + \text{OH}(^2\Pi)$ , remaining 7% of  $\text{H}_2\text{O}^+$ .

The ion production has been calculated for several values of  $K$ , and the asymptotic probabilities are presented in Figure 5. For  $K = 0$ , the RT coupling  $\tilde{A} \rightarrow \tilde{X}$  is negligible, and the dissociation into  $\text{OH}^+ + \text{H}$  takes place through the spin-orbit driven transition  $\tilde{A} \rightarrow \tilde{a}$ , which results in a dominance of  $\text{H}^+$  production. For  $K > 0$ , the dissociation through  $\tilde{X}$  is the dominant fragmentation channel, and the production of  $\text{OH}^+$  increases with  $K$  at expenses of the fragmentation into  $\text{H}^+$  through  $\tilde{A}$ . On the other hand, the remaining population of  $\text{H}_2\text{O}^+(\tilde{B} \ ^2\text{B}_2)$  does not change because it depends on the amount of the initial wave packet under the dissociation threshold.

Our results are in good agreement with the photoionization experimental data obtained by Tan et al.,<sup>8</sup> included as horizontal dashed lines, given that they correspond to average values over an unknown distribution of  $K$  values.

Recent experimental measurements<sup>22</sup> referred a branching ratio of 1.3 in  $\text{H}^+/\text{OH}^+$  production with dominance of  $\text{H}^+$ . We attribute this discrepancy to different initial conditions: Harbo et al.<sup>22</sup> excite low-lying vibrational states of  $\text{H}_2\text{O}^+(\tilde{B}^2\text{B}_2)$  with a 532 nm (2.33 eV) laser, while we start with a FC transition from the  $\text{H}_2\text{O}$  ground state, simulating Tan et al. experiments.

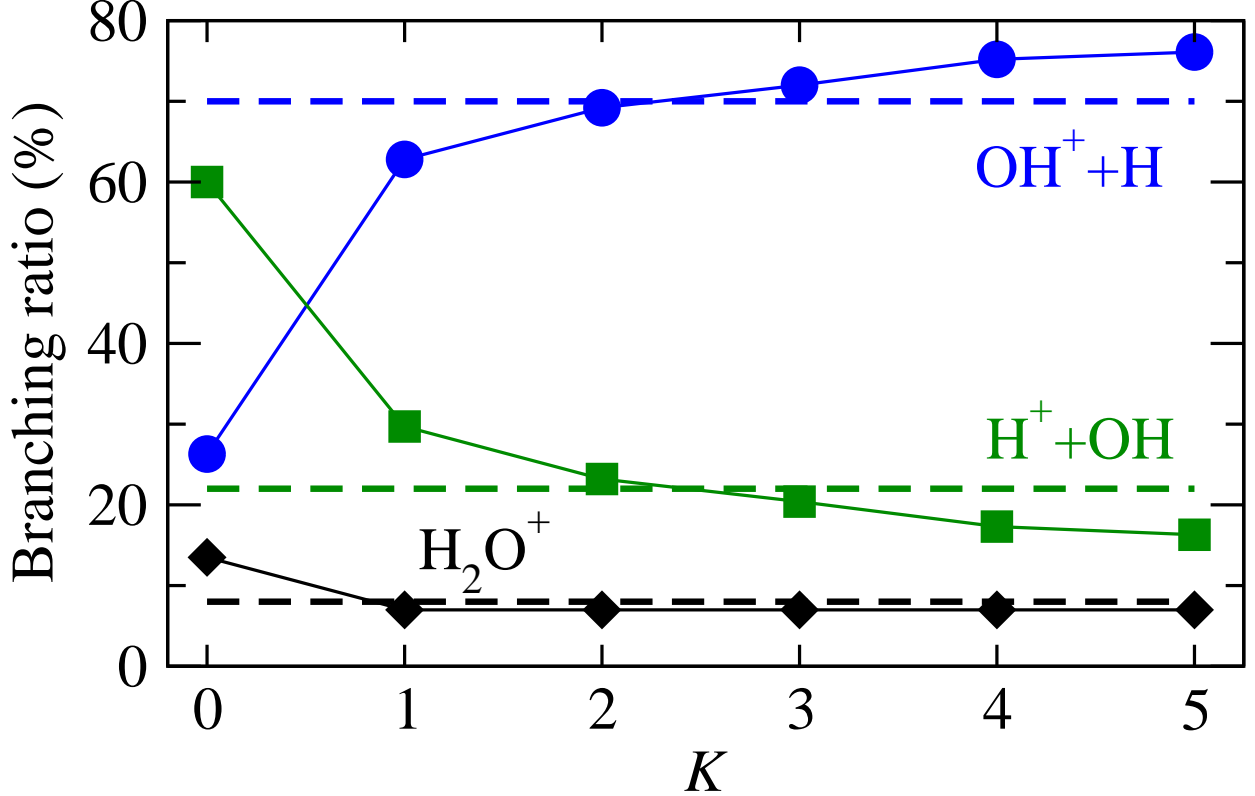


Figure 5: Branching ratios for fragmentation of  $\text{H}_2\text{O}^+$  as a function of the  $K$  quantum-number (see text). Bullets, squares and diamonds: present results. Dashed lines: experimental coefficients of  $\sigma(1b_2)$  in eqs. 1, 2 and 3.

To sum up, in this work we have implemented a wave packet, grid-based, time-propagation scheme in several potential energy surfaces, including nonadiabatic transitions between them. We have applied this method to study the fragmentation dynamics of  $\text{H}_2\text{O}^+(\tilde{B}^2\text{B}_2)$ . Four *ab initio* potential energy surfaces, and the corresponding nonadiabatic couplings, have been obtained. We have found that most of the initial wave packet in  $\tilde{B}^2\text{B}_2$  is transferred through a conical intersection to  $\tilde{A}^2\text{A}_1$  within 10 fs. We have also considered the fragmentation mech-

anism that involves spin-orbit transitions from both  $\tilde{B}^2B_2$  and  $\tilde{A}^2A_1$  states to the repulsive  $H_2O^+(\tilde{a}^4B_1)$ , but found a small ion production due to the small fraction of the wave packet that explores the relevant crossing regions in the PESs, and the small coupling. On the other hand, the inclusion of the Renner-Teller coupling between the  $\tilde{A}^2A_1$  and  $\tilde{X}^2B_1$  at linear geometries produces fragmentation branching ratios that nicely reproduce the experimental values of Tan et al..<sup>8</sup>

## Acknowledgement

This work has been partially supported by projects ENE2007-62934 and ENE2011-28200 (Secretaría de Estado de I+D+i, Spain) and the European COST actions CM1204 (XLIC) and MP1002 (Nano-IBCT). The calculations have been performed at the Centro de Computación Científica of the UAM.

## Supporting Information Available

A file is provided with an animation of the first 150 fs of wave packet propagation in the states  $\tilde{B}$ ,  $\tilde{A}$  and  $\tilde{X}$ . The probability density is indicated with a color scale. The probabilities of occupation of these states are also plotted as a function of time. The contour lines correspond to the adiabatic potentials of  $\tilde{B}$ ,  $\tilde{A}$  and  $\tilde{X}$  states (from left to right) with a constant energy difference of 0.01 hartree. The wave packet is shown as a function of the bond angle and one of the bond distances,  $r_1$ , while it has been integrated in the remaining one.

The initial wave packet is located on the  $\tilde{B}$  surface as a result of a Franck-Condon vertical transition from the ground state of  $H_2O$ . In under 10 fs, it is transferred diabatically from  $\tilde{B}$  to  $\tilde{A}$  through the conical intersection, and lands in the  $\tilde{A}$  electronic state far from the equilibrium geometry ( $\theta = 180^\circ$ ). This results in a highly excited bending motion, which is at the root of the nodal structure of the wave function regarding the bond angle degree of freedom at  $t = 30$  fs. The conspicuous cleavage brings most of the wave packet back to the open angle geometry in about 25 fs, a small fraction of it crossing the CI and repopulating

the  $\tilde{B}$  state. The population of the  $\tilde{X}$  electronic state is at this point suddenly boosted due to the Renner-Teller coupling with  $\tilde{A}$ , concentrating in the vicinity of the  $\theta = 180^\circ$  coupling region. From here on, there is a conversion from bending to stretching motion, leading to a continuous dissociation in both  $\tilde{A}$  and  $\tilde{X}$  electronic states. This material is available free of charge via the Internet at <http://pubs.acs.org/>.

## References

- (1) Gerin, M., et al. Interstellar  $\text{OH}^+$ ,  $\text{H}_2\text{O}^+$  and  $\text{H}_3\text{O}^+$  Along the Sight-Line to G10.6–0.4. *A&A* **2010**, *518*, L110.
- (2) González-Alfonso, E., et al. Excited  $\text{OH}^+$ ,  $\text{H}_2\text{O}^+$ , and  $\text{H}_3\text{O}^+$  in NGC 4418 and Arp 220. *A&A* **2013**, *550*, A25.
- (3) Larsson, M.; Geppert, W. D.; Nyman, G. Ion Chemistry in Space. *Reports on Progress in Physics* **2012**, *75*, 066901.
- (4) Shematovich, V. Ionization Chemistry in  $\text{H}_2\text{O}$ -Dominated Atmospheres of Icy Moons. *Solar System Research* **2008**, *42*, 473–487.
- (5) Olivera, G. H.; Caraby, C.; Jardin, P.; Cassimi, A.; Adoui, L.; Gervais, B. Multiple Ionization in the Earlier Stages of Water Radiolysis. *Physics in Medicine and Biology* **1998**, *43*, 2347–2360.
- (6) Illescas, C.; Errea, L. F.; Méndez, L.; Pons, B.; Rabadán, I.; Riera, A. Classical Treatment of Ion- $\text{H}_2\text{O}$  Collisions with a Three-Center Model Potential. *Phys. Rev. A* **2011**, *83*, 052704.
- (7) Murakami, M.; Kirchner, T.; Horbatsch, M.; Lüdde, H. J. Single and Multiple Electron Removal Processes in Proton–Water-Molecule Collisions. *Phys. Rev. A* **2012**, *85*, 052704.

- (8) Tan, K. H.; Brion, C. E.; Van der Leeuw, P. E.; Van der Wiel, M. J. Absolute Oscillator Strengths (10–60 eV) for the Photoabsorption, Photoionisation and Fragmentation of  $\text{H}_2\text{O}$ . *Chem. Phys.* **1978**, *29*, 299–309.
- (9) Werner, U.; Beckord, K.; Becker, J.; Lutz, H. O. 3D Imaging of the Collision-Induced Coulomb Fragmentation of Water Molecules. *Phys. Rev. Lett.* **1995**, *74*, 1962–1965.
- (10) Gobet, F.; Farizon, B.; Farizon, M.; Gaillard, M. J.; Carré, M.; Lezius, M.; Scheier, P.; Märk, T. D. Total, Partial, and Electron-Capture Cross Sections for Ionization of Water Vapor by 20–150 keV Protons. *Phys. Rev. Lett.* **2001**, *86*, 3751–3754.
- (11) Luna, H.; Montenegro, E. C. Fragmentation of Water by Heavy Ions. *Phys. Rev. Lett.* **2005**, *94*, 043201.
- (12) Luna, H.; de Barros, A. L. F.; Wyer, J. A.; Scully, S. W. J.; Lecointre, J.; Garcia, P. M. Y.; Sigaud, G. M.; Santos, A. C. F.; Senthil, V.; Shah, M. B.; Latimer, C. J.; Montenegro, E. C. Water-Molecule Dissociation by Proton and Hydrogen Impact. *Phys. Rev. A* **2007**, *75*, 042711.
- (13) Fiquet-Fayard, F.; Guyon, P. Préionisation et Prédissociation dans la Dissociation des Molécules Triatomiques par Impact électronique. *Mol. Phys.* **1966**, *11*, 17–30.
- (14) Lorquet, A.; Lorquet, J. Excited States of Gaseous Ions. V. The Predissociation of the  $\text{H}_2\text{O}^+$  Ion. *Chem. Phys.* **1974**, *4*, 353 – 367.
- (15) Eland, J. The Predissociations of Water Ions. *Chem. Phys.* **1975**, *11*, 41 – 47.
- (16) Brundle, C. R.; Turner, D. W. High Resolution Molecular Photoelectron Spectroscopy. II. Water and Deuterium Oxide. *Proceedings of the Royal Society of London. Series A. Mathematical and Physical Sciences* **1968**, *307*, 27–36.
- (17) Reutt, J. E.; Wang, L. S.; Lee, Y. T.; Shirley, D. A. Molecular Beam Photoelectron



- Spectroscopy and Femtosecond Intramolecular Dynamics of  $\text{H}_2\text{O}^+$  and  $\text{D}_2\text{O}^+$ . *J. Chem. Phys.* **1986**, *85*, 6928–6939.
- (18) Eroms, M.; Jungen, M.; Meyer, H.-D. Nonadiabatic Nuclear Dynamics after Valence Ionization of  $\text{H}_2\text{O}$ . *J. Phys. Chem. A* **2010**, *114*, 9893–9901.
- (19) Dehareng, D. Intramolecular Dynamics by Photoelectron Spectroscopy. III. Predissociation of the  $\tilde{B}^2B_2$  State of  $\text{H}_2\text{O}^+$  and  $\text{D}_2\text{O}^+$  by a Semiclassical Approach. *Chemical Physics* **1986**, *110*, 375 – 389.
- (20) Powis, I.; Reynolds, D. J. Dissociation Dynamics of  $\text{D}_2\text{O}^+$  Ions Prepared in the  $B^2B_2$  State. *J. Chem. Soc., Faraday Trans.* **1991**, *87*, 921–926.
- (21) Sage, A. G.; Oliver, T. A.; Dixon, R. N.; Ashfold, M. N. Velocity Map Imaging Studies of the Photodissociation of  $\text{H}_2\text{O}^+$  Cations. *Mol. Phys.* **2010**, *108*, 945–955.
- (22) Harbo, L. S.; Dziarzhytski, S.; Domesle, C.; Brenner, G.; Wolf, A.; Pedersen, H. B. Lifetime of Low Vibrational Levels of the Metastable  $\tilde{B}^2B_2$  State of  $\text{H}_2\text{O}^+$  Probed by Photodissociation at 532 nm. *Phys. Rev. A* **2014**, *89*, 052520.
- (23) Werner, H.-J.; Knowles, P. J.; Knizia, G.; Manby, F. R.; Schütz, M. Molpro: a General Purpose Quantum Chemistry Program Package. *WIREs Comput. Mol. Sci.* **2012**, *2*, 242–253.
- (24) Barragán, P.; Errea, L. F.; Méndez, L.; Rabadán, I.; Riera, A. Electron Capture in Collisions of  $\text{N}^{2+}$  and  $\text{O}^{2+}$  Ions with  $\text{H}(1s)$  at Low Impact Energies. *Phys. Rev. A* **2006**, *74*, 024701.
- (25) Haxton, D. J.; Rescigno, T. N.; McCurdy, C. W. Dissociative Electron Attachment to the  $\text{H}_2\text{O}$  Molecule. II. Nuclear Dynamics on Coupled Electronic Surfaces Within the Local Complex Potential Model. *Phys. Rev. A* **2007**, *75*, 012711.

- (26) Haxton, D. J.; Rescigno, T. N.; McCurdy, C. W. Erratum: “Dissociative Electron Attachment to the H<sub>2</sub>O Molecule. II. Nuclear Dynamics on Coupled Electronic Surfaces within the Local Complex Potential Model” [Phys. Rev. A 75, 012711 (2007)]. *Phys. Rev. A* **2007**, 76, 049907(E).
- (27) Leforestier, C. Grid Representation of Rotating Triatomics. *J. Chem. Phys.* **1991**, 94, 6388–6397.
- (28) Carter, S.; Handy, N. A Variational Method for the Calculation of Ro-Vibronic Levels of any Orbitally Degenerate (Renner-Teller) Triatomic Molecule. *Molecular Physics* **1984**, 52, 1367–1391.
- (29) Suarez, J.; Farantos, S.; Stamatiadis, S.; Lathouwers, L. A Method for Solving the Molecular Schrödinger Equation in Cartesian Coordinates Via Angular Momentum Projection Operators. *Computer Physics Communications* **2009**, 180, 2025 – 2033.
- (30) Guantes, R.; Farantos, S. C. High Order Finite Difference Algorithms for Solving the Schrödinger Equation in Molecular Dynamics. *J. Chem. Phys.* **1999**, 111, 10827–10835.
- (31) Dundas, D.; McCann, J. F.; Parker, J. S.; Taylor, K. T. Ionization Dynamics of Laser-Driven H<sub>2</sub><sup>+</sup>. *J. Phys. B: At. Mol. Opt. Phys.* **2000**, 33, 3261.
- (32) Ma, J.; Xie, C.; Zhu, X.; Yarkony, D. R.; Xie, D.; Guo, H. Full-Dimensional Quantum Dynamics of Vibrationally Mediated Photodissociation of NH<sub>3</sub> and ND<sub>3</sub> on Coupled Ab Initio Potential Energy Surfaces: Absorption Spectra and NH<sub>2</sub>( $\tilde{A}^2A_1$ )/NH<sub>2</sub>( $\tilde{X}^2B_1$ ) Branching Ratios. *The Journal of Physical Chemistry A* **0**, 0, PMID: 25036988.